Published in final edited form as:
*Cancer Res*. 2021 October 15; 81(20): 5325–5335. doi:10.1158/0008-5472.CAN-21-1545.

# Targeting the IRE1α/XBP1 endoplasmic reticulum stress response pathway in *ARID1A*-mutant ovarian cancers

**Joseph A. Zundell**[1,2], **Takeshi Fukumoto**[1], **Jianhuang Lin**[1], **Nail Fatkhudinov**[1], **Timothy Nacarelli**[1], **Andrew V. Kossenkov**[3], **Qin Liu**[4], **Joel Cassel**[5], **Chih-Chi Andrew Hu**[6], **Shuai Wu**[1,*], **Rugang Zhang**[1,*]

[1]Immunology, Microenvironment & Metastasis Program, The Wistar Institute, Philadelphia, PA 19104, USA

[2]Department of Biological Sciences, Misher College of Arts and Sciences, University of Science, Philadelphia, PA 19104, USA

[3]Gene Expression and Regulation Program, The Wistar Institute, Philadelphia, PA 19104, USA

[4]Molecular and Cellular Oncogenesis Program, The Wistar Institute, Philadelphia, PA 19104, USA

[5]Molecular Screening and Protein Expression Facility, The Wistar Institute, Philadelphia, PA 19104, USA

[6]Center for Translational Research in Hematologic Malignancies, Houston Methodist Cancer Center, Houston Methodist Research Institute, Houston, TX 77030, USA

## Abstract

The SWI/SNF chromatin remodeling complex is frequently altered in human cancers. For example, the SWI/SNF component *ARID1A* is mutated in more than 50% of ovarian clear cell carcinomas (OCCC), for which effective treatments are lacking. Here we report that ARID1A transcriptionally represses the IRE1α-XBP1 axis of the endoplasmic reticulum (ER) stress response, which confers sensitivity to inhibition of the IRE1α-XBP1 pathway in *ARID1A*-mutant OCCC. *ARID1A* mutational status correlated with response to inhibition of the IRE1α-XBP1 pathway. In a conditional $Arid1a^{flox/flox}/Pik3ca^{H1047R}$ genetic mouse model, *Xbp1* knockout significantly improved survival of mice bearing OCCCs. Furthermore, the IRE1α inhibitor B-I09 suppressed the growth of ARID1A-inactivated OCCCs *in vivo* in orthotopic xenograft, patient-derived xenograft, and the genetic mouse models. Finally, B-I09 synergized with inhibition of HDAC6, a known regulator of the ER stress response, in suppressing the growth of *ARID1A*-inactivated OCCCs. These studies define the IRE1α-XBP1 axis of the ER stress response as a targetable vulnerability for *ARID1A*-mutant OCCCs, revealing a promising therapeutic approach for treating *ARID1A*-mutant ovarian cancers.

---

[*]Correspondence should be addressed to: **Rugang Zhang, Ph.D.**, The Wistar Institute, 3601 Spruce Street, Philadelphia, PA 19104, Tel: 215-495-6840, rzhang@wistar.org, or, **Shuai Wu, Ph.D.**, The Wistar Institute, 3601 Spruce Street, Philadelphia, PA 19104, Tel: 215-495-6841, swu@wistar.org.

**Conflicts of Interest Statement:** The authors declare no conflicts of interest.

## Introduction

ARID1A epigenetically regulates gene expression via the SWI/SNF chromatin-remodeling complex by controlling gene accessibility (1,2). SWI/SNF complexes contribute to both gene activation and repression in a context-dependent manner (3). *ARID1A* has one of the highest mutation rates across many cancer types (4–6). In fact, based on statistical saturation analyses, *ARID1A* is among the top 10 most mutated genes and is the most frequently mutated epigenetic regulator across all human cancers (5,6). Notably, *ARID1A* is mutated in >50 % of ovarian clear cell carcinoma (OCCC) (7–9). Over 90% of the *ARID1A* mutations observed in epithelial ovarian cancer are frameshift or nonsense mutations that result in the loss of ARID1A protein expression (7,9,10). The loss of ARID1A correlates with late-stage disease and predicts early recurrence (11). OCCC is generally refractory to platinum-based chemotherapy, and when diagnosed at advanced stages, carries the worst prognosis among all histosubtypes of ovarian cancer (12). Therefore, there is an even greater need for novel therapeutic approaches that are selective for *ARID1A*-mutated ovarian cancer.

Upon detecting endoplasmic reticulum (ER) stress, the unfolded protein response (UPR) orchestrates adaptive programs to promote cancer cell survival (13–15). Thus, inhibition of the UPR represents a therapeutic approach for cancers with hyperactive ER stress response (15). The mammalian UPR is governed by three stress transducers that sense ER stress. They include inositol-required enzyme alpha (IRE1α), activating transcription factor 6 (ATF6) and protein kinase RNA-like ER kinase (PERK) (15). IRE1α signaling is the most conserved and well-studied UPR. In response to ER stress, IRE1α signaling involves a conformational change that activates its RNase domain (15). IRE1α processes the mRNA encoding the transcription factor X-box binding protein 1 (XBP1) by excising a 26-nucleotide intron in the *XBP1* mRNA (15). This splicing event shifts the coding reading frame, leading to the translation of a transcription factor termed XBP1s to promote cell survival by resolving ER stress (15). However, the role of SWI/SNF complex in regulating ER stress response has never been explored.

Therapeutic resistance typically enables cancer cells to escape the effects of single agent treatment. Combinatorial therapeutic strategies offer a solution for this major challenge (16). Histone deacetylase 6 (HDAC6) is a class IIb HDAC isoenzyme (17). Unlike other HDACs, HDAC6 primarily functions in the cytoplasm and targets non-histone proteins (18). Notably, HDAC6 regulates the degradation of misfolded proteins through aggresomes and cells deficient in HDAC6 are hypersensitive to the accumulation of unfolded proteins (19). HDAC6 inhibition is selective against *ARID1A* inactivation and inhibition of HDAC6 activity using the clinically applicable small molecule inhibitor ACY1215 reduced the tumor burden of established *ARID1A*-mutant, but not wild-type, ovarian tumors (20). However, whether HDAC6 inhibition synergizes with ER stress response inhibition in *ARID1A*-mutated cancers has never been explored. Here we show that ARID1A transcriptionally represses the IRE1α-XBP1 axis of the ER stress response and pharmacological inhibition of the IRE1α-XBP1 pathway alone or in combination with HDAC6 inhibition represents an urgently needed therapeutic strategy for *ARID1A*-mutant OCCCs.

# Materials and Methods

## Cell Lines and Culture Conditions

The ovarian cancer cell lines OVCA429 (RRID:CVCL_3936), OVTOKO (JCRB Cat# NIHS0301, RRID:CVCL_3117), SKOV3 (JCRB Cat# NIHS0737, RRID:CVCL_4Y20), OVISE (JCRB Cat# JCRB1043, RRID:CVCL_3116), and TOV21G (ATCC Cat# CRL-11730, RRID:CVCL_3613) were cultured in RPMI 1640 supplemented with 10% FBS at 37 °C and supplied with 5% $CO_2$. RMG1 (JCRB Cat# JCRB0172, RRID:CVCL_1662) and KK (RRID:CVCL_F844) cell lines were cultured in 1:1 Dulbecco's modified Eagle medium DMEM/F12 supplemented with 10% FBS at 37 °C and supplied with 5% $CO_2$. Endogenously FLAG-tagged ARID1A and ARID1A knockout RMG1 cells were constructed and cultured as we previously published (21). ARID1B knockout RMG1 cells were generated and cultured as we previously published (22). Primary ovarian clear cell carcinoma cells (VOA4841 and XVOA295) were produced as described previously (20) and cultured in RPMI 1640 supplemented with 10% FBS at 37 °C and supplied with 5% $CO_2$. The protocol for using primary cultures of human ovarian clear cell tumor cells was approved by the University of British Columbia Institutional Review Board (H18–01652). Written informed consent was obtained from human participants. All relevant ethical regulations have been complied with. OVTOKO, SKOV3, OVISE, and RMG1 were purchased from JCRB. TOV21G was purchased from the ATCC. OVCA429 and KK cell lines were obtained from Dr. Ie-Ming Shih. Monthly mycoplasma testing was performed on all cell lines using the LookOut Mycoplasma PCR detection kit (Sigma). All cell lines used for experimentation were passaged less than 30 times and authenticated at the Wistar Institute's Genomics Facility using short tandem repeat DNA profiling.

## Antibodies and Reagents

Antibodies against rabbit anti-ARID1A (3 μg ChIP, abcam,182560,), rabbit anti-ARID1A (1:1000 immunoblot, cell signaling, 12354, RRID:AB_2637010), mouse anti-RNA Pol II (2 μg ChIP, SantaCruz, sc-47701x, RRID:AB_677353), mouse anti-FLAG (3 μg ChIP, 1:1000 immunoblot, Millipore Sigma, F3165, RRID:AB_259529), mouse anti-β-Actin (1:10,000 immunoblot, Millipore Sigma, A1978, RRID:AB_476692), rabbit anti-ARID1B (1:1000 immunoblot, abgent, AT1190a, RRID:AB_1551334), rabbit anti-XBP1 (1:1000 immunoblot, Cell Signaling, 12782, RRID:AB_2687943), rabbit anti-SNF5 (3 μg ChIP, Bethyl, A301–087A, RRID:AB_2191714), rabbit anti-cleaved PARP (1:1000 immunoblot, Cell Signaling, 5625, RRID:AB_10699459), rabbit anti-c-MYC (1:1000 immunoblot, cell signaling, 5605, RRID:AB_1903938), mouse anti-Ki67 (1:1000 IHC, cell signaling, 9449, RRID:AB_2797703), rabbit anti-cleaved caspase 3 (1:200 IHC, 1:1000 immunoblot, cell signaling, 9661, RRID:AB_2341188), mouse anti-ATF6 (1:1000 immunoblot, abcam, 122897, RRID:AB_10899171), rabbit anti-PERK (1:1000 immunoblot, cell signaling, 3192, RRID:AB_2095847), and rabbit anti-ATF4 (1:1000 immunoblot, cell signaling, 11815, RRID:AB_2616025), rabbit anti-acetylated-α-Tubulin (1:1000 immunoblot, cell signaling, 5335, RRID:AB_10544694), and rabbit anti-CHOP (1:1000 immunoblot, cell signaling, 2895, RRID:AB_2089254) were purchased commercially. Rabbit anti-phospho-PERK antibody was kindly provided by Dr. Costantinos Koumenis at the University of Pennsylvania. Tunicamycin (3516) and B-I09 (6009) were purchased from

Tocris Bioscience. Thapsigargin (T9033), GSK2656157 (504651) and MG-132 (C2211) were purchased from Sigma-Aldrich. CeapinA7 (2323027–38-7) was purchased from MedChemExpress. 4μ8c (B1874) was purchased from APExBIO. ACY1215 (S8001) was purchased from Selleck-chem. B-I09 was provided by Dr. Chih-Chi Andrew Hu and synthesized as previously published (23).

## Protein Isolation and immunoblotting

Cells were lysed using RIPA buffer (1% NP-40, 0.5% sodium deoxycholate, 0.1% SDS, 150mM NaCl, 1mM EDTA, and 10mM Tris-HCl, pH 7.4) containing Roche complete protease inhibitors. Protein concentrations were determined by Bradford assays (BioRad). Samples were boiled in SDS-PAGE sample buffer (2% SDS, 200mM sucrose, 2mM EDTA, 0.1% bromophenol blue, and 62.5mM Tris-HCl, pH 6.9) with β-mercaptoethanol and proteins were resolved by SDS-PAGE. Resolved proteins were transferred to nitrocellulose (BioRad) or polyvinylidene fluoride membranes (Millipore) and blocked in 5% w/v nonfat milk in TBS-T. Immunoblotting was performed with the indicated primary antibodies and their appropriate horseradish peroxidase-conjugated secondary antibodies. Immunoblots were developed using SuperSignal West Pico PLUS and femto chemiluminescent substrates (Thermo Fisher Scientific).

## Chromatin immunoprecipitation (ChIP)

Cells were cultured until 70–80% confluency and then 1% formaldehyde crosslinker was added for 10 minutes at room temperature. Formaldehyde reactions were then quenched by 0.125M glycine for 5 minutes. Next, cells were washed with PBS once and then collected into appropriate conical tubes. The samples were centrifuged at 400 relative centrifugal force (RCF) and PBS was aspirated away from the cell pellet. Then an appropriate volume of PBS was added to the cell pellet to transfer the fixed cells to a 1.5mL microcentrifuge tube. The sample was centrifuged again at 400 RCF and the PBS was aspirated away from the cell pellet prior to cell lysis. Fixed cells were lysed using ChIP lysis buffer 1 (50 mM HEPES-KOH (pH 7.5), 140 mM NaCl, 1 mM EDTA (pH 8.0), 1% Triton X-100, and 0.1% DOC) on ice for 10 minutes, centrifuged at 1,000 RCF and then supernatant was aspirated. Then, ChIP lysis buffer 2 (10 mM Tris (pH 8.0), 200 mM NaCl, 1 mM EDTA, and 0.5 mM EGTA) was added at room temperature for 10 minutes, centrifuged at 1,000 RCF and then supernatant was aspirated. Chromatin was digested with MNase (cell signaling, 10011) in digestion buffer (10 mM Tris 8.0, 1 mM $CaCl_2$, and 0.2% Triton X-100) at 37 °C for 15 min. The sample was then centrifuged ≥16,000 RCF at 4 °C for 1 minute. The supernatant was then extracted to a new 1.5mL microcentrifuge tube, NaCl was added to 100mM, and placed on ice. The remaining nuclear pellet was disrupted by two pulses of the Bioruptor (Diagenode) under high output in 0.4mL of ChIP lysis buffer 3 (10mM Tris-HCl (pH 8.0), 100mM NaCl, 1mM EDTA, 0.5mM EGTA, 0.1% ODC, and 0.5% N-lauroylsarcosine). The lysed nuclear pellet sample was then combined with the supernatant from the previous step and centrifuged at ≥16,000 RCF at 4 °C for 10 minutes. The supernatant was transferred to a new 1.5mL microcentrifuge tube and DNA was quantified using the NanoDrop (ThermoFisher Scientific). All samples contained the same amount of DNA and antibody per immunoprecipitation and were compared to IgG isotype controls. 1% input was taken for ChIP-qPCR quantitation. Samples were incubated on a tube rocker over night at 4 °C with the appropriate antibody. The following day, protein A/G magnetic Dynabeads (ThermoFisher Scientific, 10002D/10003D) were added to each sample and incubated at 4 °C for 1 hour on the tube rocker. Then, all samples were washed twice with ChIP lysis buffer 1, ChIP lysis buffer 1 with 0.65M NaCl, and wash buffer (10mM Tris-HCl (pH 8.0), 250mM LiCl, 0.5% NP-40, 0.5% DOC, and 1mM EDTA (pH 8.0)). TE (50mM Tris-HCl (pH 8.0), 10mM EDTA (pH 8.0)) was added to the samples and the beads were transferred to a new tube to reduce background signal. Lastly, samples (including 1% input) were eluted with TE supplemented with 1% SDS on a ThermoMixer (Eppendorf) at 65 °C at 1000 RPM for 15 minutes. Crosslinks were then reversed by adding NaCl and proteinase K to final concentrations of 200mM and 0.3μg/μl, respectively. Samples were incubated at 65 °C for 3 hours, cooled, and DNA was purified using the ChIP DNA Clean and Concentrator Kit (Zymo Research). Purified ChIP DNA was analyzed by qPCR using iTaq Universal SYBR Green Supermix (BioRad).

For ChIP-qPCR the following primers were used:

*XBP1* locus forward: 5’-CGACCTCATGTCCGAGTTAAG-3’ and reverse 5’-ACTCTCTCGTTAGAGATGACCA-3’; *ERN1* locus forward: 5’-CAGGGCAAGTGGCAGAA-3’ and reverse 5’-GCGCTTCGAATCCTTGTTTG-3’.

## Reverse Transcriptase quantitative PCR

Total RNA was isolated using TRIzol reagent (Invitrogen). Complimentary DNA was produced using iTaq Universal SYBR Green One-step kit (BioRad). RNA expression was determined using the QuantStudio 3 Real-Time PCR system (ThermoFisher Scientific) with the following sets of primers: h*ERN1* forward 5’-CCCATCAACCTCTCTTCTGTATC-3’ and reverse 5’-AGGCCGCATAGTCAAAGTAG-3’; h*XBP1s* forward 5’-CCGCAGCAGGTGCAGG-3’ and reverse 5’-GAGTCAATACCGCCAGAATCCA-3’; h*XBP1u* forward 5’-GCGCTGTCTTAACTCCTGGT-3’ and reverse 5’-GCCTCTTATGAACTTTCTTCCAG-3’; h*18s* forward 5’-AACTTTCGATGGTAGTCGCCG-3’ and reverse 5’-CCTTGGATGTGGTAGCCGTTT-3’. 18s expression was used as an internal control. To determine *Xbp1* mRNA expression in mice tumor samples the following sets of primers were used: m*Xbp1* forward 5’-GCAGACTGCTCGAGATAGAAAG-3’ and reverse 5’-AGCTGGAGTTTGTGGTTCTC-3’; mβ-Actin forward 5’-GAGGTATCCTGACCCTGAAGTA-3’ and reverse 5’-CACACGCAGCTCATTGTAGA-3’.

## Colony Formation

Cells were seeded in 24 well plates according to their growth rates. Fresh culture media containing the appropriate drug concentration was added to each well. Media containing the appropriate drug concentration was changed every three days up to twelve days. On the final day, cells were washed once with PBS, fixed, and stained with a 0.05% crystal violet, 10% methanol solution for 10 minutes. To calculate $IC_{50}$ values, integrated density was determined using NIH ImageJ software (version 1.52v).

## Immunohistochemistry

Tissue samples were paraffin embedded and sliced onto glass microscopy slides by the Histotechnology Facility at The Wistar Institute. Immunohistochemical staining was performed on consecutive tissue sections. Using the EnVision+ HRP and peroxidase (DAB) systems (DAKO Corporation) protein tissue expression was determined following manufacturer’s instructions. Stained proteins were scored using histological scoring (H score). The H score was calculated upon the intensity and frequency of the stain.

## Genotyping *Arid1a*$^{flox/flox}$/*Pik3ca*$^{H1047R}$ and *Arid1a*$^{flox/flox}$/*Pik3ca*$^{H1047R}$/*Xbp1*$^{flox/flox}$ genetic mouse model

2mm tips of mice tails were digested by proteinase K and DNA was purified. Purified mouse tail DNA was subjected to PCR using Platinum Hot start PCR Master Mix (2x) (ThermoFisher, 13000012). The PCR cycle parameters are as follows for the indicated genes:

*loxP-Xbp1*: 1) 94°C for 4min, 2) 94°C for 30s, 3) 60°C for 30s, 4) 72°C for 30s, 5) Go to step 2, 34x, 6) 72°C for 2min, 7) 12°C infinitely; *loxP-Arid1a* and wild-type/mutant *Pik3ca*: 1) 94°C for 4min, 2) 94°C for 30s, 3) 55°C for 30s, 4) 72°C for 1min, 5) Go to step 2, 34x, 6) 72°C for 5min, 7) 12°C infinitely. The following primer sets were used to amplify the indicated genes:

*Xbp1*: forward 5’- ACTTGCACCAACACTTGCCATTTC-3’ and reverse 5’-CAAGGTGGTTCACTGCCTGTAATG-3’; *Arid1a:* forward 5’-GTAATGGGAAAGCGACTACTGGAG

−3’ and reverse 5’-TGTTCATTTTTGTGGCGGGAG-3’; *Pik3ca:* forward 5’-AAAGTCGCTCTGAGTTGTTAT-3’ and reverse wild type 5’-GGAGCGGGAGAAATGGATATG-3’ and reverse mutant 5’-GCGAAGAGTTTGTCCTCAACC-3’

## Orthotopic and genetic mouse models of OCCCs

All experimental protocols were approved by the Wistar Institutional Animal Care and Use Committee (IACUC). All mice were maintained in specific pathogen-free barrier facilities. To establish patient-derived xenograft (PDX) tumors, patient samples were acquired from Christiana Hospital and deidentified as we previously described (22,24). Samples were cut into small pieces and implanted intrabursally into immunocompromised 6–10-week-old female mice. Tumors were allowed to grow, be removed, and redistributed intrabursally amongst mice for multiple generations. Once established and validated by genomic sequencing to carry *ARID1A* frame-shift mutations, which result in loss-of-expression, tumors were removed and distributed intrabursally amongst 6 mice per group. 6 months after intrabursal distribution the tumors were large enough to be randomized into two groups. Mice were treated with vehicle control (DMSO) or B-I09 (50mg/kg daily, i.p.) for two weeks.

To establish cell line-derived tumors, $1 \times 10^6$ RMG1 or TOV21G cells were unilaterally injected into the ovarian bursa sac of 6–10-week-old female mice (n=10 per group) (25).

Two weeks after intrabursal injection, mice were randomized into two groups and treated with vehicle control (DMSO) or B-I09 (50mg/kg daily, i.p.) for two weeks. At the end of both experiments, ovarian tissue was surgically removed, and tumor burden was assessed based upon tumor weight.

Transgenic mice with latent mutations in *Arid1a* and *Pik3ca* were generated by crossing $Arid1a^{flox/flox}$ mice (kindly provided by Dr. Wang, U. Michigan and crossed onto a C57BL/6J background for 9 generations) with $R26\text{-}Pik3ca^{H1047R}$ mice carrying inducible *Pik3ca* mutations (Jackson Laboratory, Jax#016977) as we and others previously published (20,26). In these models, adenovirus-Cre intrabursal injection induces ovarian clear cell carcinoma in ~45 days. To achieve the $Arid1a^{flox/flox}/Pik3ca^{H1047R}/Xbp1^{flox/flox}$ genotype, $Xbp1^{flox/flox}$ mice (23) (kindly provided by Dr. Chih-Chi Andrew Hu) were crossed with the $Arid1a^{-/-}/Pik3ca^{H1047R}$ mice. All mice were genotyped prior to experimentation to validate their genotypes. To induce tumor growth 6–8-week-old female mice were injected intrabursally with adenovirus-Cre. For drug treatment studies, mice were randomized prior to treatment with B-I09 (50mg/kg) or vehicle control (DMSO). For synergy studies between B-I09 and ACY1215 mice were treated with 25 mg/kg of each compound. Mice were treated for five-day intervals with two days of rest between treatment intervals up to twenty-one days. Following drug treatment mice were sacrificed, and reproductive tracts were removed. Tumor weights of the injected ovary were weighed and reported.

## RNA-sequencing (RNA-seq)

RNA was extracted with Trizol (Invitrogen) for all RNA preparations, then subsequently cleaned and DNase treated using RNeasy columns (Qiagen). DNase-treated RNA was subjected to library preparation. Libraries for RNA-Seq were prepared with ScriptSeq complete Gold kit (Epicenter) and subjected to a 75 bp paired-end sequencing run on NextSeq 500, using Illumina’s NextSeq 500 high output sequencing kit following the manufacturer’s instructions.

RNA-seq data were aligned using bowtie2 (RRID:SCR_016368) (27) against the hg19 version of the human genome, and RSEM v1.2.12 software (RRID:SCR_013027) (28) was used to estimate raw read counts and Reads Per Kilobase of transcript, per Million (RPKM) using the Ensemble transcriptome. DESeq2 (RRID:SCR_015687) (29) was used to estimate the significance of differential expression between group pairs. Overall gene expression changes were considered significant if they passed FDR thresholds of <5%.

For analysis of previously published ARID1A ChIP-seq (30), genes which had ARID1A peaks within 1500 base pairs from the transcription start site (TSS) were considered. Significance of overlap was tested using hypergeometric test using 22, 184 Ensemble genes with detected expression in the RNA-seq experiment as a population size. Gene set enrichment analysis of gene sets was done using QIAGEN’s Ingenuity® Pathway Analysis software (IPA®, QIAGEN Redwood City, www.qiagen.com/ingenuity, RRID:SCR_008653) using “Diseases & Functions” options and FDR < 5% results were considered significant.

Statistical analyses were performed using GraphPad Prism 8 (GraphPad, RRID:SCR_002798) for Mac OS. Quantitative data are expressed as mean ± SD unless otherwise stated in figure legends. Drug synergy analyses were conducted by Qin Liu within the Biostatistics Unit of the Wistar Institute. Analysis of variance (ANOVA) with Fisher's least significant difference was used to identify significant differences in multiple comparisons. For all statistical analyses, the level of significance was set at 0.05.

To evaluate if there is an overall significant synergistic effect and at which dose levels the combination could reach significant synergistic effect, we calculated Interaction index with 95% confidence interval (CI) in overall as well as at various doses of each studied drug when it was combined with the other drug using Bliss independence model (31). Interaction index<1 indicates synergistic effect, and the vertical bar below the line of 1.0 indicates significant synergistic effect

### Data Availability

The following previously published datasets were used in the presented studies: ARID1A ChIP-seq: GSE104545 (30); RNA Pol II ChIP-seq: GSE120060 (21) and GSE106665 (32); ATAC-seq: GSE101966 (33), GSE124224 (34) and GSE106665 (32); and gene expression microarray: GSE6008 (35) and GSE29450 (36). The newly generated RNA-seq datasets were deposited into the Gene Expression Omnibus (GEO, RRID:SCR_005012) database can be accessed by the accession number GSE180468.

## Results

### ARID1A represses the IRE1α/XBP1s pathway

To determine whether ARID1A regulates ER stress response genes, we profiled changes in gene expression by RNA-seq in control and *ARID1A*-knockout RMG1 cells treated with or without the ER stress inducer Tunicamycin (Tu). In addition, we cross-referenced an ARID1A ChIP-seq dataset in ARID1A wildtype RMG1 cells that we previously published (21) with the RNA-seq datasets (Fig. 1A). Notably, ARID1A knockdown does not affect cell growth (20,37). The ARID1A-containing SWI/SNF complex either activates or represses gene expression in a context-dependent manner (3). Compared with its function as a transcriptional activator, ARID1A's role in repressing its target genes is less well understood. Thus, we focused our analysis on genes that are upregulated by ARID1A knockout. The analysis revealed that the ER stress response was significantly enriched amongst ARID1A-regulated direct target genes (Fig. 1A and Supplementary Fig. S1A). Notably, inactivation of another SWI/SNF subunit SMARCB1, also known as SNF5, in malignant rhabdoid tumor activates the UPR response through upregulating the MYC protein (38). However, MYC expression was not affected by *ARID1A* knockout (Supplementary Fig. S1B). This suggests new mechanisms underlying the observed activation of the ER stress response/UPR in *ARID1A* knockout cells.

We next sought to validate these findings. We showed that there was an increase in phosphorylated PERK and spliced XBP1 by *ARID1A* knockout (Supplementary Fig. S1C). Similar observations were also made in ARID1B knockout RMG1 cells compared with controls (Supplementary Fig. S1D). This suggests that the observed changes may be SWI/SNF-complex dependent. In contrast, *ARID1A* knockout did not increase the expression of either ATF4 or ATF6 (Supplementary Fig. S1C). Given the fact that IRE1α/XBP1 signaling is the most conserved UPR pathway and XBP1 plays a critical role in mediating the UPR response (15), we focused our analyses on XBP1. Upregulation of both spliced and unspliced forms of XBP1 were confirmed at both mRNA and protein levels with or without ER stress inducers such as Tu, MG-132 and Thapsigargin (Tg) (Fig. 1B–D, Supplementary S1E–F). Similar observations were also made in *ARID1A* wildtype control and the matched isogenic ARID1A knockout OVCA429 OCCC cells (Supplementary Fig. S1G–H). This suggests that these findings are not cell line specific. We next directly correlated the *ARID1A* mutational status with *XBP1* mRNA expression in The Cancer Genome Atlas (TCGA) cancer types such as uterine corpus endometrial carcinomas which display high *ARID1A* mutation frequencies (~30% cases with *ARID1A* mutation), as the TCGA does not have OCCC datasets. Compared with *ARID1A* wildtype tumors, *XBP1* mRNA was expressed at significantly higher levels in *ARID1A*-mutant tumors (Fig. 1E). Notably, *ARID1A* mutation correlates with an increase in expression of the majority of canonical IRE1α-XBP1s target genes identified in a previous study (39) (Supplementary Table S1). Likewise, in two independently published microarray datasets, compared with normal ovary or ovarian surface epithelium, expression of the majority of identified ARID1A-regulated direct genes implicated in ER stress responses were higher in OCCCs (Supplementary Fig. S1I–J) (35,36).

Our analysis of previously published ChIP-seq datasets (30) revealed that ARID1A directly bound to the promoter regions of the *ERN1* and *XBP1* genes (Fig. 2A and Supplementary S2A). Consistent with the notion that ARID1A functions as a transcriptional repressor in this context, *ARID1A* knockout increased the expression and the association of RNA polymerase II (RNA Pol II) with the promoters of both *XBP1* and *ERN1* genes in our previously published datasets (21) (Fig. 1B, 2B and Supplementary S2B–C). We validated the association of ARID1A and SNF5, a core subunit of the SWI/SNF complex, with the promoters by ChIP-qPCR analyses. These associations were reduced by *ARID1A* knockout, indicating the specificity of our analyses (Fig. 2C). To further validate these findings, we tagged the endogenous *ARID1A* locus with a FLAG epitope using CRISPR (Fig. 2D). ChIP-qPCR analyses in these cells revealed an association of FLAG-tagged ARID1A with both XBP1 and ERN1 promoters (Fig. 2E and Supplementary S2D). Consistently, data mining of the published assay for transposase-accessible chromatin using sequencing (ATAC-seq) revealed that *ARID1A* knockout increased the accessibility to the promoters of the *XBP1* and *ERN1* genes (32–34) (Supplementary Fig. S2E–F). Likewise, the association of RNA Pol II with the promoters of the XBP1 and ERN1 genes were increased by *ARID1A* knockout (21,32) (Supplementary Fig. S2G). Together, we conclude that ARID1A represses the IRE1α/XBP1 pathway of the ER stress response/UPR.

## Sensitization to inhibition of the IRE1α/XBP1 pathway by *ARID1A* inactivation

Since we show that ARID1A inactivation upregulates the IRE1α/XBP1 pathway, we next sought to determine whether inhibition of the IRE1α/XBP1 pathway is selective against *ARID1A*-inactivated cells. Toward this goal, we treated control and *ARID1A* knockout RMG1 cells with a selective IRE1α RNase inhibitor B-I09 (23). We chose B-I09 for our study because of its ability to specifically target IRE1α RNase activity and its strong safety profile *in vivo* in preclinical studies (23,40–42). Compared with controls, *ARID1A* knockout decreased the $IC_{50}$ of B-I09 in RMG1 cells (Fig. 3A–B). Consistent with the notion that unresolved ER stress leads to apoptosis, B-I09 induces apoptosis in *ARID1A* knockout RMG1 cells in a dose-dependent manner as evidenced by upregulation of apoptotic markers such as cleaved PARP p85 and cleaved Caspase 3 (Fig. 3C). As a control, B-I09 was not effective in inducing apoptosis in *ARID1A* wildtype RMG1 controls (Fig. 3C). Similarly, compared with *ARID1A* wildtype RMG1 cells, *ARID1A*-mutant TOV21G OCCC cells were sensitive to apoptotic induction by B-I09 (Supplementary Fig. S3A). Likewise, B-I09 is more effective in inducing apoptosis in *ARID1A*-mutant compared with wildtype primary OCCC cultures (Fig. 3D). Additionally, in a panel of OCCC cells, the $IC_{50}$ of B-I09 was significantly lower in *ARID1A*-mutant cells (OVISE, SKOV3, OVTOKO and TOV21G) compared with *ARID1A* wildtype cells (RMG1, OVCA429 and KK) (Fig. 3E). Similar findings were also made using another IRE1α RNase inhibitor 4μ8c (Supplementary Fig. S3B). In contrast, there was no statistical difference in $IC_{50}$ of the PERK inhibitor GSK2656157 (43) or ATF6 inhibitor CeapinA7 (44,45) between *ARID1A*-mutant and wildtype cell lines (Supplementary Fig. S3C–D). Together, these findings support that *ARID1A* inactivated cells are selectively sensitive to inhibition of the IRE1α/XBP1 pathway by inducing apoptosis.

## *Xbp1* knockout suppresses *Arid1a* deficient OCCC

Since we show that inhibition of the IRE1α/XBP1 pathway suppresses the growth of *ARID1A*-mutant OCCC cells, we sought to determine whether inactivation of the XBP1 pathway is tumor suppressive in ARID1A inactivated OCCC *in vivo*. Toward this goal, we crossed $Arid1a^{flox/flox}/Pik3ca^{H1047R}$ genetic OCCC model (20,46) with a conditional $Xbp1^{flox/flox}$ model (23) to generate the $Arid1a^{flox/flox}/Pik3ca^{H1047R}/Xbp1^{flox/flox}$ model (Supplementary Fig. S4A). To inactivate *Arid1a* and *Xbp1*, and induce $Pik3ca^{H1047R}$ expression, adeno-cre was intrabursally administered as previously reported (20). To determine the effects of *Xbp1* knockout on tumor burden, we measured the tumor weight 6 weeks after tumor induction (Supplementary Fig. S4B–C). We show that *Xbp1* knockout significantly decreased the weight of tumors developed in the $Arid1a^{-/-}/Pik3ca^{H1047R}$ model (Fig. 4A–B). Consistently, *Xbp1* knockout significantly improved the survival of mice bearing the $Arid1a/Pik3ca^{H1047R}$ tumors (Fig. 4C). Together, we conclude that *Xbp1* knockout reduces the tumor burden and improves the survival of mice bearing *Arid1a*-inactivated OCCCs.

## The IRE1α RNase inhibitor B-I09 is effective against *ARID1A*-inactivated OCCC

We next sought to determine the therapeutic potential of targeting the IRE1α/XBP1 pathway in *ARID1A*-mutant tumors. Toward this goal, we used three different mouse models. First, we used orthotopic xenograft models formed by *ARID1A*-mutant TOV21G OCCC cells. Briefly, the orthotopically transplanted cells were allowed to grow for one week to establish the orthotopic tumors (Supplementary Fig. S5A). Mice were then randomized and treated for two weeks with vehicle control or B-I09 (50 mg/kg, i.p.), the same dose as previously reported (23). We used tumor weight as a surrogate for tumor burden. Our results show that the B-I09 treatment significantly reduced the burden of orthotopic xenografts formed by *ARID1A*-mutant cells (Fig. 5A–B). Notably, the observed tumor suppressive effects by B-I09 treatment are *ARID1A* status dependent. For example, B-I09 did not significantly affect the growth of tumors formed by *ARID1A* wildtype control RMG1 cells (Supplementary Fig. S5B–C). Furthermore, B-I09 significantly reduced the expression of the cell proliferation marker Ki67 in tumors formed by *ARID1A*-mutant TOV21G but not *ARID1A* wildtype RMG1 cells (Fig. 5C–D and Supplementary S5D–E). In contrast, expression of the apoptosis marker cleaved caspase 3 was induced by B-I09 treatment in tumors formed by *ARID1A*-mutant TOV21G cells but not *ARID1A* wildtype RMG1 cells (Fig. 5C–D and Supplementary S5D–E).

We next sought to expand these studies into *ARID1A*-mutant OCCC patient-derived xenografts (Supplementary Fig. S5F–G). B-I09 significantly reduced the tumor burden in *ARID1A*-mutated OCCC PDXs (Fig. 5E–F). Likewise, B-I09 significantly reduced the tumor burden in *Arid1a*-inactivated OCCCs developed in the genetic $Arid1a^{-/-}/Pik3ca^{H1047R}$ models (Fig. 5G–H and Supplementary S5H). The reduction in tumor burden by B-I09 treatment correlated with an improvement of the survival of tumor bearing mice (Fig. 5I). To validate the *in vivo* on target effects, we examined the protein expression of spliced Xbp1 (Xbp1s) in vehicle control and B-I09 treated mice by immunoblotting. B-I09 treatment decreased Xbp1s protein expression *in vivo* (Fig. 5J–K). This result confirmed the on-target effects of B-I09. Consistent with previous reports, B-I09 was well tolerated *in vivo*. For example, B-I09 treatment did not affect the body weight of the treated tumor-bearing mice (Supplementary Fig. S5I). Thus, we conclude that the IRE1α RNase inhibitor B-I09 is effective in treating *ARID1A*-inactivated OCCCs.

### IRE1α and HDAC6 inhibitors are synergistic in suppressing ARID1A-inactivated OCCC

Inhibition of HDAC6 activity is effective against *ARID1A*-mutant cancers (20). Notably, HDAC6 plays an important role in clearing misfolded proteins and inhibition of HDAC6 activity sensitizes cells to UPR (20,47,48). This raises the possibility that IRE1α and HDAC6 inhibitors may synergize with each other in suppressing ARID1A-inactivated cells. Toward testing this possibility, we performed a contour plot analysis using a serial dilution of the IRE1α RNase inhibitor B-I09 and the HDAC6 inhibitor ACY1215. We calculated an overall significant synergistic effect based on interaction index with 95% confidence interval (CI). The analysis indicated an overall significant synergistic effect in combining B-I09 and ACY1215 (Supplementary Fig. S6A). Consistently, B-I09 and ACY1215 combination is synergistic in inducing expression of apoptotic markers such as cleaved caspase 3 and cleaved PARP p85 in *ARID1A*-mutant TOV21G cells (Fig. 6A). Notably, compared with *ARID1A* wildtype RMG1 cells, the synergy in inducing expression of these apoptotic markers was enhanced by *ARID1A* knockout (Fig. 6B). This suggests that the combination is more effective in *ARID1A*-inactivated cells. Interestingly, ACY1215 increased phospho-PERK expression (Fig. 6C), which is consistent with the notion that HDAC6 inhibition increases ER stress. In addition, ACY1215 decreases XBP1s expression in ARID1A inactivated cells (Supplementary Fig. S6B). These results are consistent with the notion that ACY1215 simultaneously increases ER stress and suppresses the XBP1s mediated ER-stress response.

We next sought to test the combination *in vivo* in the genetic $Arid1a^{-/-}/Pik3ca^{H1047R}$ mouse model. Notably, we reduced the dose of both B-I09 and ACY1215 to 25 mg/kg to allow for the observation of synergy *in vivo*. Under these conditions, although neither B-I09 nor ACY1215 alone demonstrated a significant inhibition on tumor growth compared with vehicle controls, the combination decreased tumor weight in Log10 unit by 0.62 more than the sum of single agent effects (Fig. 6D–E). From interaction effect analyses, the combination effect is significantly better in inhibiting tumor growth than the sum of single agent effects (P = 0.002), which indicates a synergistic effect. Furthermore, the combination of B-I09 and ACY1215 improved the survival of tumor bearing mice significantly compared to individual treatments alone (Fig. 6F). The combination at the doses used here were well tolerated *in vivo*. For example, the combination treatment did not significantly affect the body weight of the treated tumor-bearing mice (Supplementary Fig. S6C). Consistently, the combination did not visibly change the histological morphology of liver and kidney (Supplementary Fig. S6D). Together, we conclude that the IRE1α inhibitor B-I09 synergizes with the HDAC6 inhibitor ACY1215 in suppressing the growth of *ARID1A*-inactivated OCCC to improve the survival of tumor-bearing mice.

## Discussion

Here we show that ARID1A represses the IRE1α/XBP1 pathway of the ER stress response. This is consistent with the notion that ARID1A functions as a tumor suppressor and its inactivation promotes the survival of cancer cells by upregulating the ER stress response to adapt within the harsh tumor microenvironment. We speculate that the increase in the IRE1α-XBP1 signaling is cytoprotective due to its role in dealing with an overall increase in ER stress as evidenced by an increase in both IRE1α-XBP1 and PERK pathways of the ER stress response. Consequently, ARID1A loss creates a dependence on the upregulated IRE1α-XBP1 pathway and inhibition of this pathway is tumor suppressive in ARID1A inactivated tumors by decreasing their ability to adapt to ER stress.

Interestingly, ARID1A represses *ERN1* and *ARID1A* inactivation upregulates *ERN1* transcriptionally. In addition, ARID1A directly represses *XBP1* transcription. Thus, *ARID1A* inactivation upregulates the IRE1α/XBP1 pathway by upregulating both the substrate (XBP1) and enzyme (IRE1α) that produces the XBP1s transcription factor. In addition to the IRE1α/XBP1 pathway, the PERK pathway was also activated by *ARID1A* knockout. However, there is no selectivity against *ARID1A* mutation among cell lines by PERK inhibition. Regardless, future studies will elucidate the contributions of the PERK pathway in promoting the survival of *ARID1A*-mutant cancer cells.

Our data show that ARID1A inactivation increases XBP1s expression, which correlates with the observed hypersensitivity to B-I09 treatment. Notably, HDAC6 inhibition reduces XBP1s expression in ARID1A inactivated cells. These results suggest a model whereby HDAC6 and IRE1α inhibition converges on the inhibition of XBP1s as a potential mechanism for the observed synergy. In addition, HDAC6 inhibition increases the expression of phospho-PERK, indicating that HDAC6 inhibition increases ER stress in ARID1A-inactivated cells. Thus, HDAC6 inhibition simultaneously increases ER stress and suppresses ER stress response via downregulating XBP1s.

Epigenetic regulators can control multiple specific pathways simultaneously. For example, *ARID1A* mutation inactivates the p53 tumor suppressive pathway through upregulating HDAC6 (20), while increasing the IRE1α/XBP1 pathway as reported here. Indeed, a combination of the HDAC6 inhibition and IRE1α inhibition synergistically suppresses *ARID1A*-mutant cancers. Thus, epigenetic dysregulations are ideally suited for developing combinatorial therapeutic strategies to prevent and/or overcome therapy resistance. Notably, in addition to tumor intrinsic function, ER stress responses such as the IRE1α/XBP1 pathway are implicated in intratumoral immune cells (13,14). For example, activation of the IRE1α/XBP1 pathway is known to be immune suppressive in various populations of immune cells (13). Thus, targeting ER stress responses may reinvigorate endogenous anti-tumor immunity, which could synergize with immunotherapies such as immune checkpoint blockade (13). Since ARID1A represses PD-L1 expression and *ARID1A* mutation correlates with an increase in PD-L1 expression (49,50), it would be interesting to examine whether IRE1α inhibition also synergizes with immune checkpoint blockade in *ARID1A*-mutant cancers.

A limitation of our study is that in addition to regulating the UPR or ER stress response, HDAC6 is implicated in multiple biological processes and pathways including protein trafficking and degradation, cell shape and migration (18). Thus, in addition to regulating the ER stress response, other mechanisms regulated by HDAC6 may also contribute to the observed synergy between the HDAC6 inhibitor ACY1215 and the IRE1α inhibitor B-I09. In summary, our findings establish that pharmacological inhibition of the IRE1α/XBP1 pathway of the ER stress response alone or in combination with HDAC6 inhibitor represents a novel therapeutic strategy for *ARID1A*-mutated cancers.

## Supplementary Material

Refer to Web version on PubMed Central for supplementary material.

## Acknowledgements

We thank Mr. X. Hua for assistance with intrabursal injection procedures, Dr. B. Keith for critical reading of the manuscript, and Dr. David Huntsman for providing the primary cultures of ovarian clear cell carcinomas. This work was supported by US National Institutes of Health grants (R01CA202919, R01CA239128, R01CA260661 and P50CA228991 to R.Z.; R01CA163910 and R01CA190860 to C.C.A.H.; and F31CA247336 to J.Z.), US Department of Defense (OC180109 and OC190181 to R.Z.), The Honorable Tina Brozman Foundation for Ovarian Cancer Research and The Tina Brozman Ovarian Cancer Research Consortium 2.0 (to R.Z.), and the Ovarian Cancer Research Alliance [Collaborative Research Development Grant #596552 to R.Z. and Ann and Sol Schreiber Mentored Investigator Award #649658 to J.L.]. Support of Core Facilities was provided by Cancer Centre Support Grant (CCSG) CA010815 to The Wistar Institute.

## References

1. Wang W, Xue Y, Zhou S, Kuo A, Cairns BR, Crabtree GR. Diversity and specialization of mammalian SWI/SNF complexes. Genes & development 1996;10:2117–30 [PubMed: 8804307]
2. Sif S, Saurin AJ, Imbalzano AN, Kingston RE. Purification and characterization of mSin3A-containing Brg1 and hBrm chromatin remodeling complexes. Genes & development 2001;15:603–18 [PubMed: 11238380]
3. Wilson BG, Roberts CW. SWI/SNF nucleosome remodellers and cancer. Nature reviews Cancer 2011;11:481–92 [PubMed: 21654818]

4. Wu JN, Roberts CW. ARID1A mutations in cancer: another epigenetic tumor suppressor? Cancer discovery 2013;3:35–43 [PubMed: 23208470]
5. Lawrence MS, Stojanov P, Mermel CH, Robinson JT, Garraway LA, Golub TR, et al. Discovery and saturation analysis of cancer genes across 21 tumour types. Nature 2014;505:495–501 [PubMed: 24390350]
6. Bailey MH, Tokheim C, Porta-Pardo E, Sengupta S, Bertrand D, Weerasinghe A, et al. Comprehensive Characterization of Cancer Driver Genes and Mutations. Cell 2018;173:371–85 e18 [PubMed: 29625053]
7. Jones S, Wang TL, Shih Ie M, Mao TL, Nakayama K, Roden R, et al. Frequent mutations of chromatin remodeling gene ARID1A in ovarian clear cell carcinoma. Science 2010;330:228–31 [PubMed: 20826764]
8. Murakami R, Matsumura N, Brown JB, Higasa K, Tsutsumi T, Kamada M, et al. Exome Sequencing Landscape Analysis in Ovarian Clear Cell Carcinoma Shed Light on Key Chromosomal Regions and Mutation Gene Networks. Am J Pathol 2017;187:2246–58 [PubMed: 28888422]
9. Wiegand KC, Shah SP, Al-Agha OM, Zhao Y, Tse K, Zeng T, et al. ARID1A mutations in endometriosis-associated ovarian carcinomas. N Engl J Med 2010;363:1532–43 [PubMed: 20942669]
10. Guan B, Gao M, Wu CH, Wang TL, Shih Ie M. Functional analysis of in-frame indel ARID1A mutations reveals new regulatory mechanisms of its tumor suppressor functions. Neoplasia 2012;14:986–93 [PubMed: 23097632]
11. Ye S, Yang J, You Y, Cao D, Huang H, Wu M, et al. Clinicopathologic Significance of HNF-1beta, AIRD1A, and PIK3CA Expression in Ovarian Clear Cell Carcinoma: A Tissue Microarray Study of 130 Cases. Medicine (Baltimore) 2016;95:e3003
12. Mackay HJ, Brady MF, Oza AM, Reuss A, Pujade-Lauraine E, Swart AM, et al. Prognostic relevance of uncommon ovarian histology in women with stage III/IV epithelial ovarian cancer. Int J Gynecol Cancer 2010;20:945–52 [PubMed: 20683400]
13. Song M, Cubillos-Ruiz JR. Endoplasmic Reticulum Stress Responses in Intratumoral Immune Cells: Implications for Cancer Immunotherapy. Trends Immunol 2019;40:128–41 [PubMed: 30612925]
14. Cubillos-Ruiz JR, Bettigole SE, Glimcher LH. Tumorigenic and Immunosuppressive Effects of Endoplasmic Reticulum Stress in Cancer. Cell 2017;168:692–706 [PubMed: 28187289]
15. Urra H, Dufey E, Avril T, Chevet E, Hetz C. Endoplasmic Reticulum Stress and the Hallmarks of Cancer. Trends Cancer 2016;2:252–62 [PubMed: 28741511]
16. Kaelin WG, Jr. The concept of synthetic lethality in the context of anticancer therapy. Nature reviews Cancer 2005;5:689–98 [PubMed: 16110319]
17. de Ruijter AJ, van Gennip AH, Caron HN, Kemp S, van Kuilenburg AB. Histone deacetylases (HDACs): characterization of the classical HDAC family. Biochem J 2003;370:737–49 [PubMed: 12429021]
18. Pulya S, Amin SA, Adhikari N, Biswas S, Jha T, Ghosh B. HDAC6 as privileged target in drug discovery: A perspective. Pharmacol Res 2021;163:105274
19. Kawaguchi Y, Kovacs JJ, McLaurin A, Vance JM, Ito A, Yao TP. The deacetylase HDAC6 regulates aggresome formation and cell viability in response to misfolded protein stress. Cell 2003;115:727–38 [PubMed: 14675537]
20. Bitler BG, Wu S, Park PH, Hai Y, Aird KM, Wang Y, et al. ARID1A-mutated ovarian cancers depend on HDAC6 activity. Nat Cell Biol 2017;19:962–73 [PubMed: 28737768]
21. Wu S, Fatkhutdinov N, Rosin L, Luppino JM, Iwasaki O, Tanizawa H, et al. ARID1A spatially partitions interphase chromosomes. Sci Adv 2019;5:eaaw5294
22. Wu S, Fukumoto T, Lin J, Nacarelli T, Wang Y, Ong D, et al. Targeting glutamine dependence through GLS1 inhibition suppresses ARID1A-inactivated clear cell ovarian carcinoma. Nature Cancer 2021;2:189–200 [PubMed: 34085048]
23. Tang CH, Ranatunga S, Kriss CL, Cubitt CL, Tao J, Pinilla-Ibarz JA, et al. Inhibition of ER stress-associated IRE-1/XBP-1 pathway reduces leukemic cell survival. J Clin Invest 2014;124:2585–98 [PubMed: 24812669]

24. Zhao B, Lin J, Rong L, Wu S, Deng Z, Fatkhutdinov N, et al. ARID1A promotes genomic stability through protecting telomere cohesion. Nature communications 2019;10:4067
25. Karakashev S, Zhang RG. Mouse models of epithelial ovarian cancer for preclinical studies. Zool Res 2021;42:153–60 [PubMed: 33527800]
26. Chandler RL, Damrauer JS, Raab JR, Schisler JC, Wilkerson MD, Didion JP, et al. Coexistent ARID1A-PIK3CA mutations promote ovarian clear-cell tumorigenesis through pro-tumorigenic inflammatory cytokine signalling. Nature communications 2015;6:6118
27. Langmead B, Salzberg SL. Fast gapped-read alignment with Bowtie 2. Nat Methods 2012;9:357–9 [PubMed: 22388286]
28. Li B, Dewey CN. RSEM: accurate transcript quantification from RNA-Seq data with or without a reference genome. BMC Bioinformatics 2011;12:323 [PubMed: 21816040]
29. Love MI, Huber W, Anders S. Moderated estimation of fold change and dispersion for RNA-seq data with DESeq2. Genome Biol 2014;15:550 [PubMed: 25516281]
30. Trizzino M, Barbieri E, Petracovici A, Wu S, Welsh SA, Owens TA, et al. The Tumor Suppressor ARID1A Controls Global Transcription via Pausing of RNA Polymerase II. Cell reports 2018;23:3933–45 [PubMed: 29949775]
31. Liu Q, Yin X, Languino LR, Altieri DC. Evaluation of drug combination effect using a Bliss independence dose-response surface model. Stat Biopharm Res 2018;10:112–22 [PubMed: 30881603]
32. Suryo Rahmanto Y, Shen W, Shi X, Chen X, Yu Y, Yu ZC, et al. Inactivation of Arid1a in the endometrium is associated with endometrioid tumorigenesis through transcriptional reprogramming. Nature communications 2020;11:2717
33. Kelso TWR, Porter DK, Amaral ML, Shokhirev MN, Benner C, Hargreaves DC. Chromatin accessibility underlies synthetic lethality of SWI/SNF subunits in ARID1A-mutant cancers. Elife 2017;6
34. Xu G, Chhangawala S, Cocco E, Razavi P, Cai Y, Otto JE, et al. ARID1A determines luminal identity and therapeutic response in estrogen-receptor-positive breast cancer. Nat Genet 2020;52:198–207 [PubMed: 31932695]
35. Wu R, Hendrix-Lucas N, Kuick R, Zhai Y, Schwartz DR, Akyol A, et al. Mouse model of human ovarian endometrioid adenocarcinoma based on somatic defects in the Wnt/beta-catenin and PI3K/Pten signaling pathways. Cancer Cell 2007;11:321–33 [PubMed: 17418409]
36. Stany MP, Vathipadiekal V, Ozbun L, Stone RL, Mok SC, Xue H, et al. Identification of novel therapeutic targets in microdissected clear cell ovarian cancers. PloS one 2011;6:e21121
37. Bitler BG, Aird KM, Garipov A, Li H, Amatangelo M, Kossenkov AV, et al. Synthetic lethality by targeting EZH2 methyltransferase activity in ARID1A-mutated cancers. Nat Med 2015;21:231–8 [PubMed: 25686104]
38. Carugo A, Minelli R, Sapio L, Soeung M, Carbone F, Robinson FS, et al. p53 Is a Master Regulator of Proteostasis in SMARCB1-Deficient Malignant Rhabdoid Tumors. Cancer Cell 2019;35:204–20 e9 [PubMed: 30753823]
39. Adamson B, Norman TM, Jost M, Cho MY, Nunez JK, Chen Y, et al. A Multiplexed Single-Cell CRISPR Screening Platform Enables Systematic Dissection of the Unfolded Protein Response. Cell 2016;167:1867–82 e21 [PubMed: 27984733]
40. Tang CHA, Chang S, Hashimoto A, Chen YJ, Kang CW, Mato AR, et al. Secretory IgM Exacerbates Tumor Progression by Inducing Accumulations of MDSCs in Mice. Cancer Immunol Res 2018;6:696–710 [PubMed: 29650518]
41. Xie H, Tang CH, Song JH, Mancuso A, Del Valle JR, Cao J, et al. IRE1alpha RNase-dependent lipid homeostasis promotes survival in Myc-transformed cancers. J Clin Invest 2018;128:1300–16 [PubMed: 29381485]
42. Tavernier SJ, Osorio F, Vandersarren L, Vetters J, Vanlangenakker N, Van Isterdael G, et al. Regulated IRE1-dependent mRNA decay sets the threshold for dendritic cell survival. Nat Cell Biol 2017;19:698–710 [PubMed: 28459443]
43. Atkins C, Liu Q, Minthorn E, Zhang SY, Figueroa DJ, Moss K, et al. Characterization of a novel PERK kinase inhibitor with antitumor and antiangiogenic activity. Cancer research 2013;73:1993–2002 [PubMed: 23333938]

44. Gallagher CM, Garri C, Cain EL, Ang KK, Wilson CG, Chen S, et al. Ceapins are a new class of unfolded protein response inhibitors, selectively targeting the ATF6alpha branch. Elife 2016;5
45. Gallagher CM, Walter P. Ceapins inhibit ATF6alpha signaling by selectively preventing transport of ATF6alpha to the Golgi apparatus during ER stress. Elife 2016;5
46. Chandler RL, Damrauer JS, Raab JR, Schisler JC, Wilkerson MD, Didion JP, et al. Coexistent ARID1A-PIK3CA mutations promote ovarian clear-cell tumorigenesis through pro-tumorigenic inflammatory cytokine signalling. Nature communications 2015;6:6118
47. Boyault C, Zhang Y, Fritah S, Caron C, Gilquin B, Kwon SH, et al. HDAC6 controls major cell response pathways to cytotoxic accumulation of protein aggregates. Genes & development 2007;21:2172–81 [PubMed: 17785525]
48. Cosenza M, Civallero M, Marcheselli L, Sacchi S, Pozzi S. Ricolinostat, a selective HDAC6 inhibitor, shows anti-lymphoma cell activity alone and in combination with bendamustine. Apoptosis 2017;22:827–40 [PubMed: 28315173]
49. Shen J, Ju Z, Zhao W, Wang L, Peng Y, Ge Z, et al. ARID1A deficiency promotes mutability and potentiates therapeutic antitumor immunity unleashed by immune checkpoint blockade. Nat Med 2018;24:556–62 [PubMed: 29736026]
50. Fukumoto T, Fatkhutdinov N, Zundell JA, Tcyganov EN, Nacarelli T, Karakashev S, et al. HDAC6 Inhibition Synergizes with Anti-PD-L1 Therapy in ARID1A-Inactivated Ovarian Cancer. Cancer research 2019;79:5482–9 [PubMed: 31311810]

## Statement of Significance

These findings indicate that pharmacological inhibition of the IRE1α-XBP1 pathway alone or in combination with HDAC6 inhibition represents an urgently needed therapeutic strategy for *ARID1A*-mutant ovarian cancers.

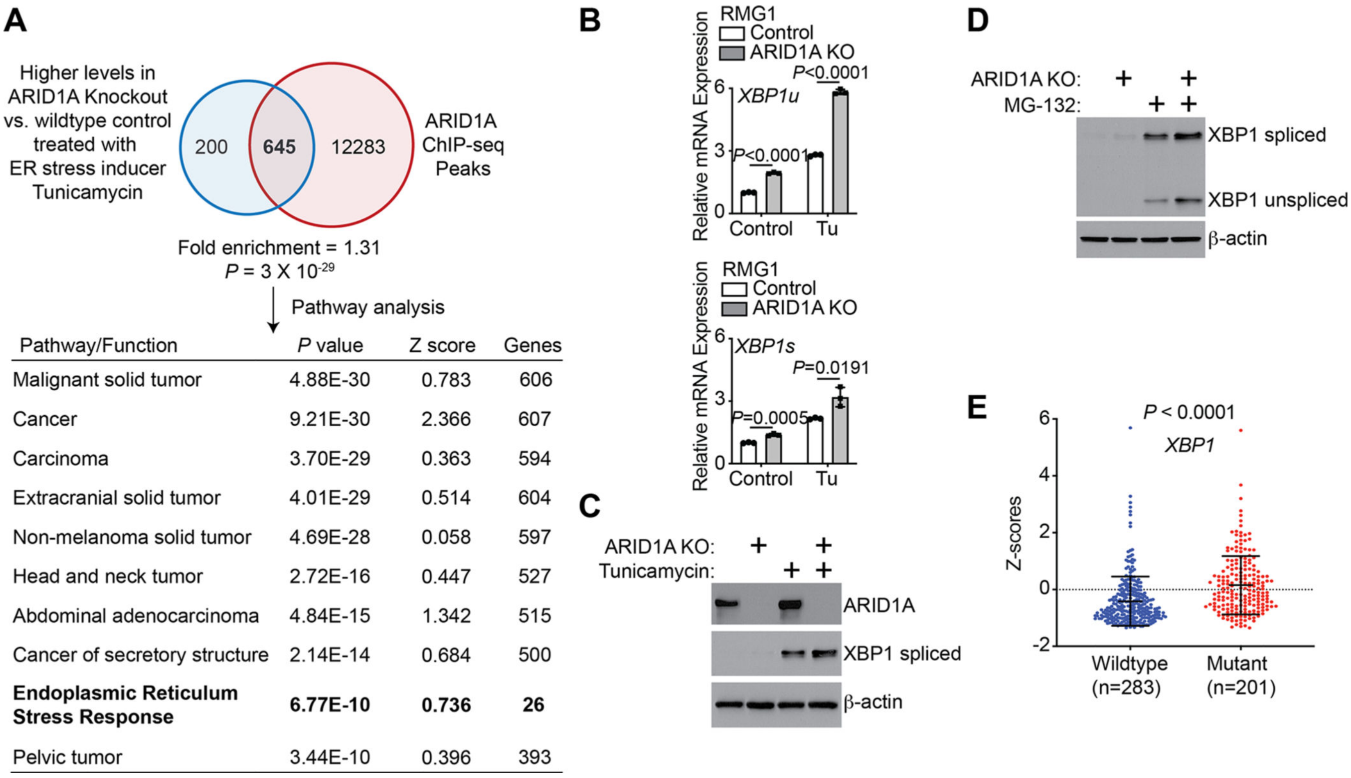

| Pathway/Function | *P* value | Z score | Genes |
|---|---|---|---|
| Malignant solid tumor | 4.88E-30 | 0.783 | 606 |
| Cancer | 9.21E-30 | 2.366 | 607 |
| Carcinoma | 3.70E-29 | 0.363 | 594 |
| Extracranial solid tumor | 4.01E-29 | 0.514 | 604 |
| Non-melanoma solid tumor | 4.69E-28 | 0.058 | 597 |
| Head and neck tumor | 2.72E-16 | 0.447 | 527 |
| Abdominal adenocarcinoma | 4.84E-15 | 1.342 | 515 |
| Cancer of secretory structure | 2.14E-14 | 0.684 | 500 |
| **Endoplasmic Reticulum Stress Response** | **6.77E-10** | **0.736** | **26** |
| Pelvic tumor | 3.44E-10 | 0.396 | 393 |

**Figure 1: ARID1A regulates XBP1 expression.**

(**A**) Experimental strategy used to identify ARID1A-regulated genes under 5μg/mL tunicamycin treatment for 4 hours in ARID1A wildtype control and ARID1A knockout RMG1 OCCC cells. Ingenuity Pathway Analysis revealed that the ER stress response is among the top 10 pathways enriched in ARID1A direct target genes upregulated by ARID1A knockout in response to tunicamycin treatment condition. (**B**) Control and ARID1A knockout RMG1 cells were treated with 5 μg/mL tunicamycin or vehicle controls for 4 hours. Expression of both unspliced *XBP1* (*XBP1u*) and spliced *XBP1* (*XBP1s*) was determined by RT-qPCR analysis. n = 3 biologically independent experiments. (**C**) Controls and ARID1A knockout RMG1 cells were treated with 5 μg/mL tunicamycin or vehicle controls for 4 hours. Expression of ARID1A, spliced XBP1 and a loading control β-actin was determined by immunoblot. (**D**) Control and ARID1A knockout RMG1 cells were treated with 20 μM MG-132 or vehicle controls for 4 hours. Expression of both unspliced and spliced XBP1 was determined by immunoblot and β-actin expression was used as a loading control. Please note that unspliced XBP1 is stabilized by MG-132 to make it detectable. (**E**) Relative expression of *XBP1* in the ARID1A wildtype (n=283) and mutated (n=201) uterine corpus endometrial carcinoma cases in the TCGA database. *P* values were calculated using two-tailed Student's *t*-test except by Fisher Exact test in A. Error bars represent mean with SD.

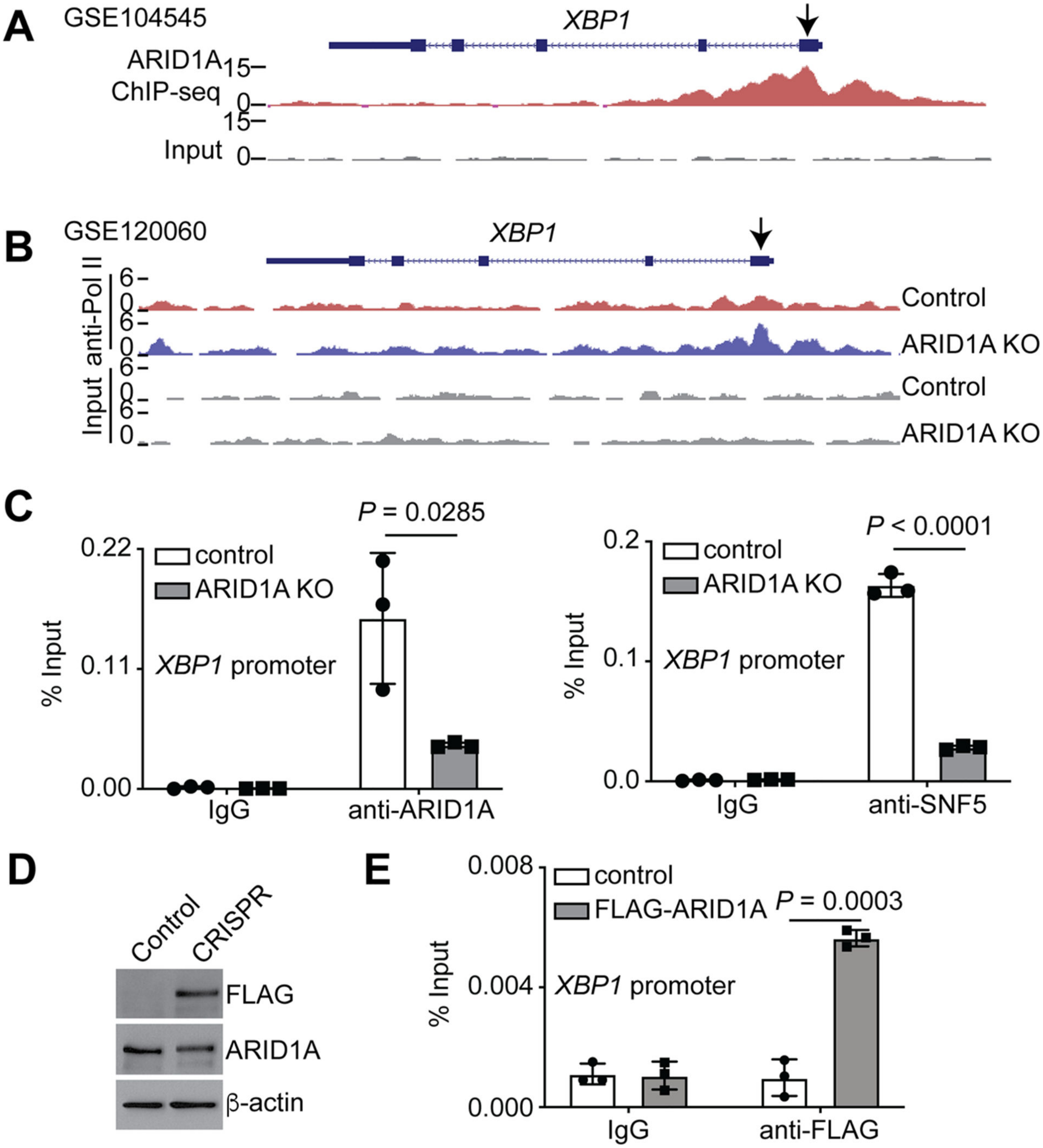

**Figure 2: ARID1A directly represses the XBP1 gene.**

(**A**) ARID1A ChIP-seq and input tracks in the *XBP1* gene locus in *ARID1A* wildtype RMG1 cells (30). (**B**) RNA polymerase II ChIP-seq and input tracks in the XBP1 gene locus in control and ARID1A knockout RMG1 cells (21). (**C**) The association of ARID1A and SNF5 with the *XBP1* gene promoter in control and *ARID1A* knockout RMG1 cells was determined by ChIP-qPCR analysis. An isotype matched IgG was used as a negative control. n = 3 biologically independent experiments. (**D**) Expression of FLAG, ARID1A and a loading control β-actin in parental control and endogenous ARID1A FLAG tagged RMG1 cells was determined by immunoblot. (**E**) The association of ARID1A with the XBP1 gene promoter in control parental and FLAG-tagged endogenous ARID1A-expressing cells was determined by ChIP-qPCR analysis. An isotype matched IgG was used as a negative control. n = 3 biologically independent experiments. *P* values were calculated using two-tailed Student's *t*-test. Error bars represent mean with SD.

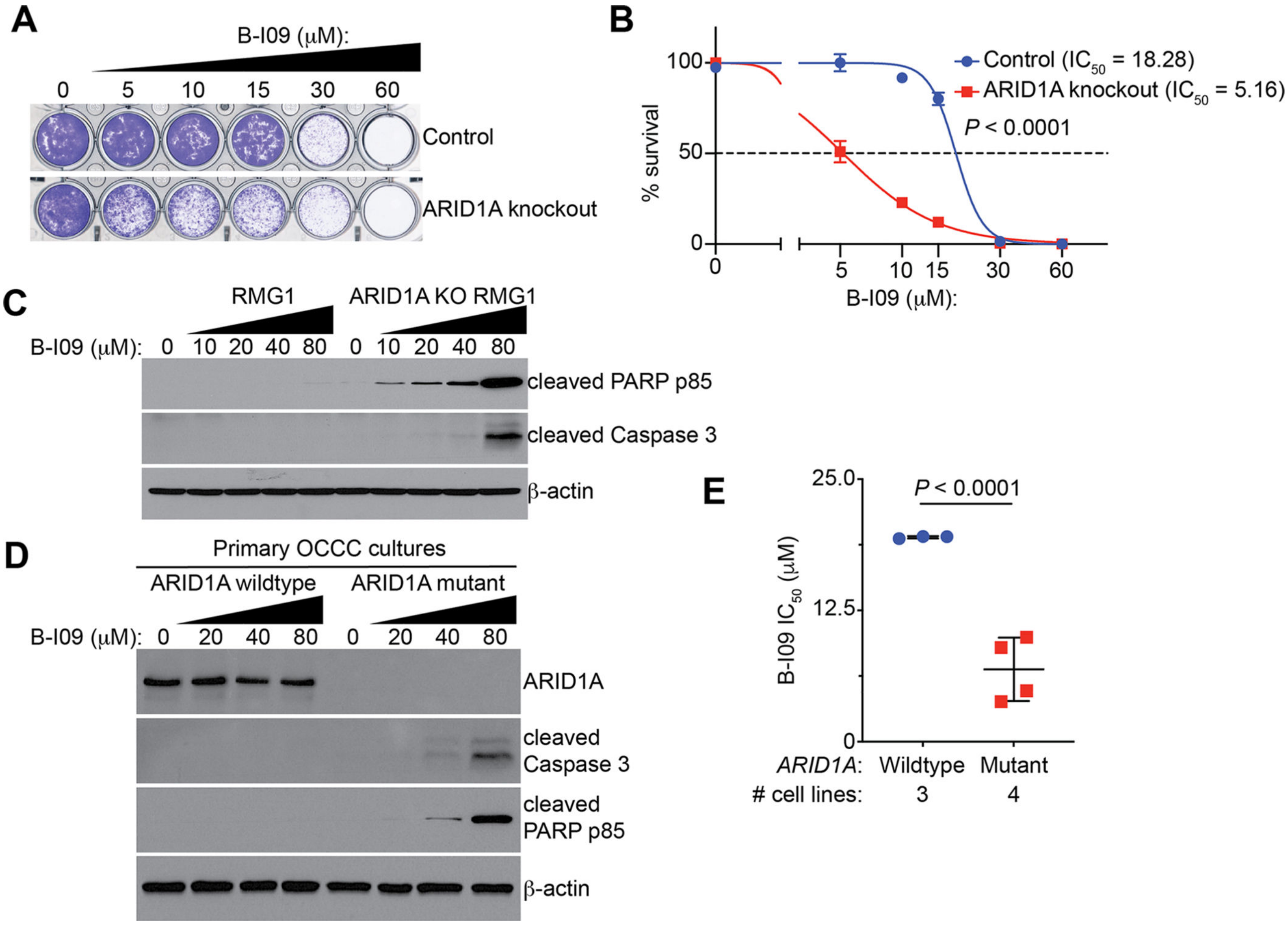

**Figure 3: ARID1A inactivation sensitizes cells to IRE1α inhibition.**

(**A**) Representative images of colony formation assay in control and ARID1A knockout RMG1 cells treated with indicated concentrations of B-I09. (**B**) Dose-response curves of indicated control and *ARID1A* knockout RMG1 cells to B-I09 were determined by colony formation assay. n = 4 biologically independent experiments. (**C**) Control and *ARID1A* knockout RMG1 cells were treated with the indicated doses of B-I09 for 24 hours. Expression of the indicated markers of apoptosis and a loading control β-actin was examined by immunoblot. (**D**) *ARID1A* wildtype and mutant primary OCCC cultures were treated with the indicated concentration of B-I09 for 24 hours. Expression of ARID1A, the indicated markers of apoptosis and a loading control β-actin was determined by immunoblot. (**E**) $IC_{50}$ of B-I09 is significantly higher in *ARID1A* wildtype (RMG1, OVCA429 and KK) than mutant (TOV21G, OVTOKO, OVISE and SKOV3) cell lines. *P* values were calculated using two-tailed Student's *t*-test. Error bars represent mean with SD.

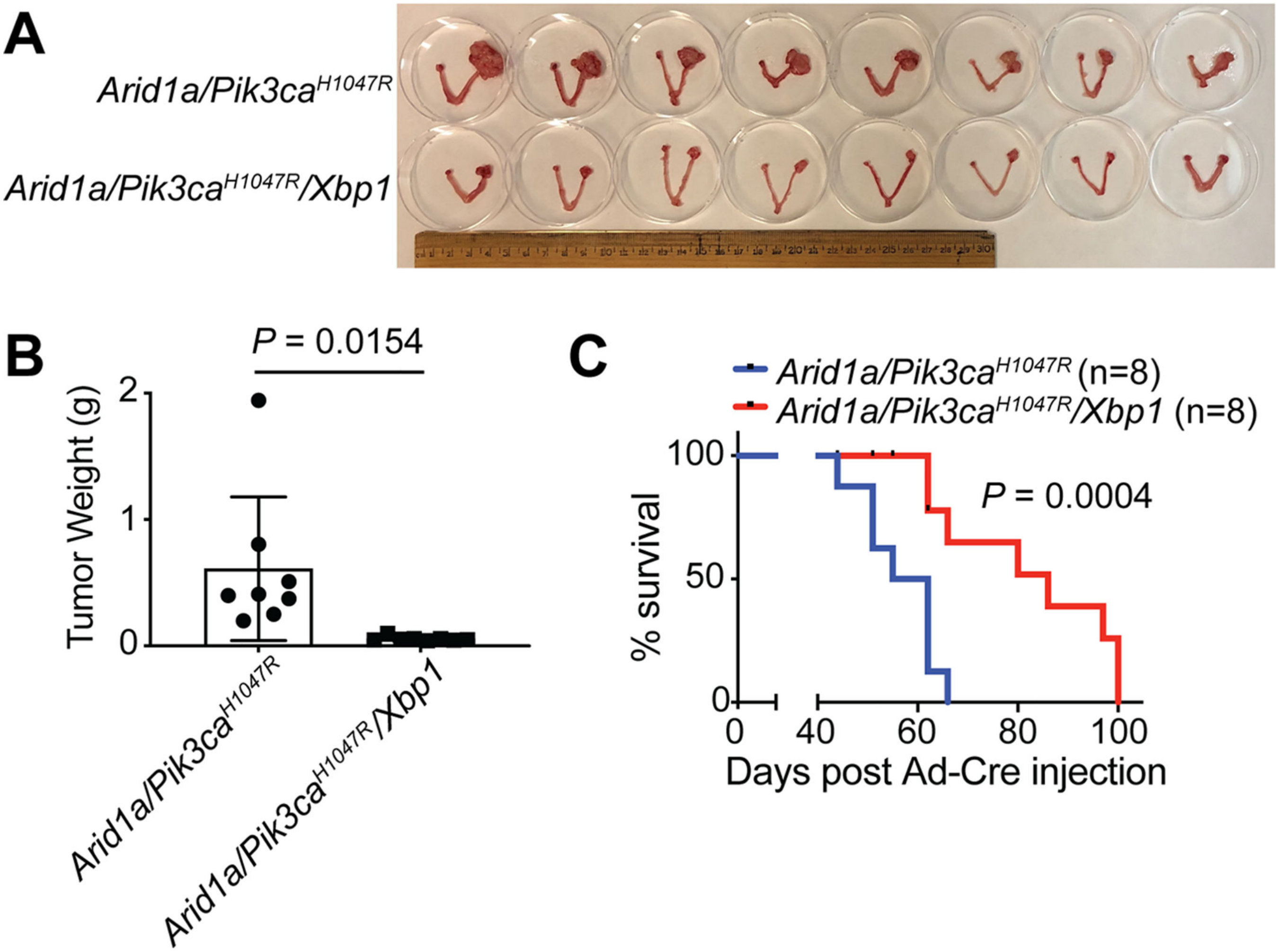

**Figure 4: *Xbp1* knockout suppresses tumorigenesis in *Arid1a*$^{-/-}$/*Pik3ca*$^{H1047R}$ genetic OCCC mouse model.**

(**A**) *Arid1a*$^{flox/flox}$/*Pik3ca*$^{H1047R}$ and *Arid1a*$^{flox/flox}$/*Pik3ca*$^{H1047R}$/*Xbp1*$^{flox/flox}$ mice were intrabursally injected with Ad-Cre to knockout *Arid1a* and/or *Xbp1* and activate *Pik3ca*$^{H1047R}$. After 6 weeks, the mice were euthanized. Shown is an image of reproductive tracts with tumors from each labeled group. (**B**) Tumor weight was quantified as a surrogate for the tumor burden in the indicated groups (n = 8 mice per group). (**C**) Mice from the indicated groups were followed for survival by the Kaplan-Meier methods (n = 8 mice per group). *P* values were calculated using two-tailed Student's *t*-test in B and log-rank test in C. Error bars represent mean with SD.

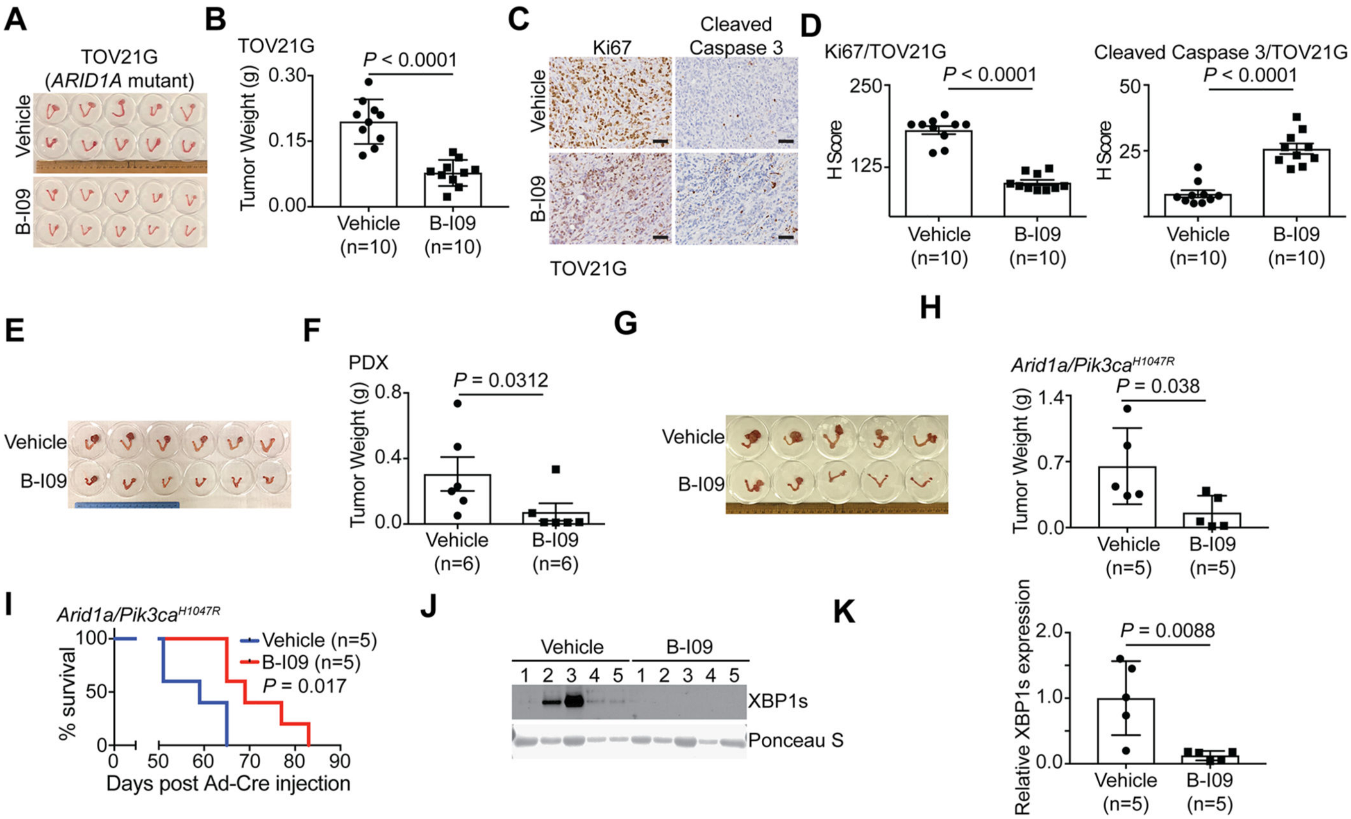

**Figure 5: B-I09 is effective against *ARID1A*-inactivated OCCCs.**

(**A-D**) Orthotopic xenografts formed by *ARID1A*-mutated TOV21G cells treated with vehicle or B-I09. Shown are images of reproductive tracks with tumors from indicated groups (**A**). Tumor weight was measured as surrogate for tumor burden (n = 10 mice per group) (**B**). Dissected tumors from the indicated treatment groups were subjected to immunohistochemical (IHC) staining for cell proliferation marker Ki67 or apoptosis marker cleaved caspase 3 on serial sections (**C**), and the histological scores (H-score) of indicated markers was quantified in each of the indicated treatment groups (**D**). Scale bar = 100 μm. (**E-F**) Mice bearing *ARID1A*-mutated OCCC PDXs were treated with vehicle or B-I09 (n = 6 mice per group). Shown are images of reproductive tracks with tumors from the indicated groups at end of treatments (**E**). Tumor weight was measured as a surrogate for tumor burden (**F**). (**G-K**) Mice bearing OCCC developed from the genetic $Arid1a^{-/-}/Pik3ca^{H1047R}$ model were treated with vehicle or B-I09 (n = 5 mice per group). Shown is an image of reproductive tracks with tumors from the indicated groups at the end of treatments (**G**). Tumor weight was measured as a surrogate for tumor burden (**H**). After stopping the treatment, mice from the indicated treatment groups were followed for survival by the Kaplan-Meier methods (n = 5 mice per group) (**I**). Expression of spliced XBP1 (XBP1s) in tumors from the indicated treatment groups was determined by immunoblot. A non-specific band revealed by Ponceau S staining was used as a loading control (**J**). The relative XBP1s expression was quantified based on intensity of immunoblot bands normalized against loading controls using NIH ImageJ software (**K**). *P* values were calculated using two-tailed Student's *t*-test except by log-rank test in I. Error bars represent mean with SD.

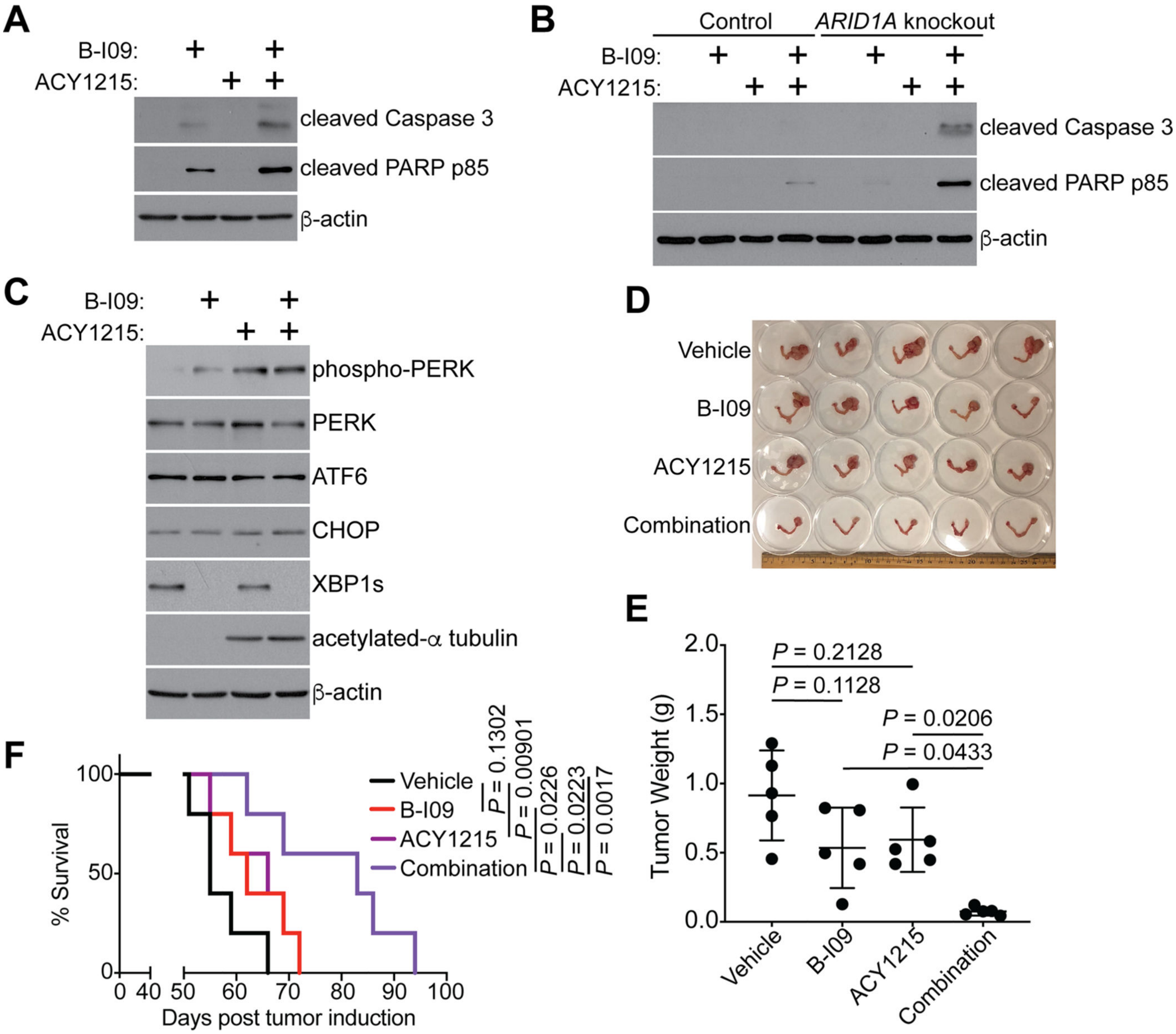

**Figure 6: IRE1α and HDAC6 inhibitors are synergistic in suppressing ARID1A-inactivated OCCCs.**

(**A**) *ARID1A*-mutated TOV21G cells were treated with the IRE1α inhibitor B-I09 (20μM), HDAC6 inhibitor ACY1215 (3 μM), or a combination for 72 hours. Expression of the indicated apoptosis markers and a loading control β-actin was examined by immunoblot. (**B**) Same as (**A**), but for control and ARID1A knockout RMG1 cells. (**C**) *ARID1A*-mutated TOV21G cells were treated with the IRE1α inhibitor B-I09 (20μM), HDAC6 inhibitor ACY1215 (3 μM), or a combination for 72 hours. Expression of the indicated apoptosis markers and a loading control β-actin was examined by immunoblot. (**D-F**) Mice bearing OCCCs developed from the genetic $Arid1a^{-/-}/Pik3ca^{H1047R}$ model were treated with B-I09 (25 mg/kg), ACY1215 (25 mg/kg) or a combination for 3 weeks (n = 5 mice per group). Shown is an image of reproductive tracks with tumors from the indicated groups at the end of treatments (**D**). Tumor weight was measured as a surrogate for tumor burden (**E**). After stopping the treatment, mice from the indicated treatment groups were followed for survival by the Kaplan-Meier methods (n = 5 mice per group) (**F**). *P* values were calculated using two-tailed Student's *t*-test in D and log-rank test in F. Error bars represent mean with SD.